Mutable Polarization Switching Characteristics in Wurtzite $Al_{1-x}Sc_xN$ Ferroelectric Films Enabled by Sc-Doping

*Youdi Gu, Shu Shi, Hanxin Su, Geng Huangfu, Lanxin Jia, Siqin Li, Kaixuan Sun, Yichen Wu, Tao Zeng, Siewlang Teo, Ming Lin, Yao Zhu, Han Wang and Jingsheng Chen**

Dr. Y. Gu, Dr. S. Shi, H. Su, Dr. G. Huangfu, L. Jia, S. Li, K. Sun, Y. Wu, Dr. T. Zeng, Prof. J. Chen
Department of Materials Science and Engineering, National University of Singapore, Singapore 117575, Singapore
E-mail: msecj@nus.edu.sg

S. Teo, Dr. M. Lin
Institute of Materials Research and Engineering (IMRE), Agency for Science, Technology and Research (A*STAR), 2 Fusionopolis Way, Innovis #08-03, Singapore 138634, Singapore

Dr. Y. Zhu
Institute of Microelectronics, Agency for Science, Technology and Research (A*STAR), Singapore 138634, Singapore

Prof. H. Wang

Shenyang National Laboratory for Materials Science, Institute of Metal Research, Chinese Academy of Sciences, Shenyang 110016, China

Keywords: aluminum scandium nitride, wurtzite ferroelectrics, mutable polarization switching kinetics, Sc doping, high-density ferroelectric memory

Abstract: **Wurtzite ferroelectric aluminum scandium nitrides ($Al_{1-x}Sc_xN$) are highly appealing for their large remanent polarization, steep hysteresis and easy integration with multiple mainstream semiconductor platforms. However, their applications are constrained by the inherently high coercive electric field (E_c), desperately needing a comprehensive research of polarization switching for potentially lowering E_c. In particular, the correlations between polarization switching mechanisms and Sc doping levels remain underexplored. Here, we investigate the polarization switching kinetics in wurtzite ferroelectric $Al_{1-x}Sc_xN$ (x = 0.25, 0.275 and 0.3) subjected to varied voltage amplitudes and pulse durations, revealing a mutable polarization switching. The $Al_{0.75}Sc_{0.25}N$ sample displays uniform switching behavior described by Kolmogorov-**

Avrami-Ishibashi (KAI) model, while the intermediate composition $Al_{0.725}Sc_{0.275}N$ exhibits transitional switching behavior, which is suitable for both KAI and nucleation-limited-switching (NLS). Especially, $Al_{0.7}Sc_{0.3}N$ with obviously reduced coercive and activation fields, exhibits a NLS mechanism. We find that higher level Sc doping generates more nucleation sites, reducing energy barriers and accelerating polarization switching, driving the transition from KAI to NLS. Energetic analysis further elucidates the doping-induced crossover of switching mechanisms. These results provide a new insight into the fundamental understanding of polarization switching in wurtzite ferroelectric nitrides, which is critical for realizing their optimal and reliable applications.

1. Introduction

Ferroelectric (FE) materials are widely used in a variety of key technologies such as non-volatile random access memories, field-effect transistors, neuromorphic memristors, sensors, and solar cells.[1–7] In 2019, Fichtner et al. reported unexpected ferroelectricity in wurtzite-structured aluminum scandium nitride ($Al_{1-x}Sc_xN$),[8] a well-known piezoelectric material. Robust ferroelectricity has since been demonstrated in other wurtzite FEs of $Al_{1-x}B_xN$, $Al_{1-x}Y_xN$, $Ga_{1-x}Sc_xN$, and $Zn_{1-x}Mg_xO$,[9–12] challenging the long-standing notion that wurtzite crystals lack switchable polarization. Compared to traditional FEs, such as perovskite-type PZT and fluorite-type $Hf_{1-x}Zr_xO_2$,[3,13–15] the extremely high remanent polarization (P_r) above 100 $\mu C/cm^2$, low processing temperatures, excellent thermal stability, a very high FE transition temperature (T_C > 1000 °C), square FE hysteresis loop and relatively easy integration with existing and emerging semiconductors (e.g., Si, GaN, SiC, AlN) are the main advantages that make wurtzite-type $Al_{1-x}Sc_xN$ attractive for memory-related applications.[3,8,16–19] However, the primary limitation lies in its inherently high E_c, which approaches the breakdown field at room temperature, increasing the FE switching energy cost and breakdown risk.[3,8,16,18,20] Addressing this challenge requires potential strategies such as alloying design,[8–12,21] strain engineering,[22–

[24] and exploration of new wurtzite FEs.[21,25,26] A deep understanding of its polarization switching process and mechanism, from atomic to micron device scales, is critical to optimizing its performance and unlocking its full potential for advanced applications.

Recent advancements have shed light on the polarization switching mechanisms of wurtzite FEs at both atomic and micrometer scale. Through *in-situ* scanning transmission electron microscopy (STEM) and first-principles calculations,[16] it was revealed that $Al_{0.94}B_{0.06}N$ adopts a disordered yet low-energy non-polar atomic configuration, facilitating the FE switching. Additionally, Lee et al. found in theory that $Al_{1-x}Sc_xN$ alloys exhibit a new switching mechanism with increasing Sc composition, enabling a low barrier pathway.[21] On the other hand, understanding polarization switching kinetics in micrometer-scale capacitors, which reveals domain nucleation, growth, and motion, is equally critical.[27]

The switching kinetics of wurtzite FEs are quiet different from that of perovskite and fluorite counterparts, remaining less explored and more debated. For example, in 2020, Fichtner et al. provided initial insights into $Al_{0.64}Sc_{0.36}N$ film switching dynamics, suggesting the classical Kolmogorov-Avrami-Ishibashi (KAI) model was applicable.[28] However, Yazawa et al. in 2023 observed an abrupt switching behavior in $Al_{0.7}Sc_{0.3}N$ and $Al_{0.94}B_{0.06}N$ under high electric fields and introduced a simultaneous non-linear nucleation and growth (SNNG) model.[29] In theory, Behrendt et al. recently proposed an FE fractal switching mechanism as the cause of anomalously fast switching in wurtzite-structured FEs.[30] Additionally, Krishnamoorthy et al. also in $Al_{1-x}Sc_xN$ theoretically found an inhomogeneous nucleation-and-growth at low fields, in contrast, a distinct nucleation-limited-switching (NLS) behavior at high fields.[31] Further experiments in 2024 corroborated the presence or dominance of NLS mechanism in $Al_{1-x}Sc_xN$.[32–34] However, little attention has been placed on studying the correlation between polarization switching kinetics mechanisms and Sc doping levels in experiments, leading to gaps in understanding the mechanism behind the reduction of E_c in $Al_{1-x}Sc_xN$ FE films. Since Sc substitutional doping in $Al_{1-x}Sc_xN$ acts as a point defect that can affect

the nucleation and growth of domains during FE switching,[31,34,35] the polarization switching mechanisms may even be completely different at different Sc doping levels.

In this work, we prepare wurtzite FE films as well as investigate the polarization switching kinetics of $Al_{1-x}Sc_xN$ (x = 0.25, 0.275 and 0.3) with different voltages and pulse lengths to systematically understand the role of Sc doping concentration on the polarization switching mechanism. Our findings indicate that the classical nucleation and domain growth mechanism, as described by the KAI model, applies to $Al_{0.75}Sc_{0.25}N$ sample with relatively lower Sc concentrations. Notably, the polarization switching behavior varies with Sc doping levels, where higher Sc content (e.g., $Al_{0.7}Sc_{0.3}N$) results in a reduced FE switching barrier and facilitates a nucleation-limited-switching mechanism. Moreover, by summarizing and comparing the reported works on the relationship between FE switching activation energy and Sc content in $Al_{1-x}Sc_xN$, a shift in the domain switching mechanism induced by Sc doping can be further supported. These valuable findings provide key insights into the future engineering of reliable applications in emerging wurtzite-nitride-based FEs.

2. Results and Discussion

2.1. Sample fabrication and structure characterizations

The sandwiched Pt/$Al_{1-x}Sc_xN$ (AlScN)/Pt films were deposited by magnetron sputtering on SiO_2/Si(100) substrates (See the Methods). **Figure 1**a is a schematic of sample stack. The sandwiched samples were deposited without breaking the vacuum condition to protect the AlScN from oxidation, which could have a detrimental impact on its FE properties.[36,37] Synchrotron X-ray diffraction (XRD) θ-2θ scans (Figure 1b) were used to analyze the out-of-plane crystal structures. The AlScN (0002) and Pt (111) diffraction (textured bottom electrode) peaks were distinct, with no impurity phases detected, confirming high *c*-axis crystallinity and the wurtzite structure of the films. The (0002) peak positions for $Al_{0.75}Sc_{0.25}N$ and $Al_{0.7}Sc_{0.3}N$ were observed at 36.02° and 35.84°, respectively, with slight differences attributed to Sc doping

levels.[38] The intensity of wurtzite (0002) peak is higher when doping Sc content is lower, which is also in agreement with prior studies.[38,39] X-ray rocking curves (omega scans) further evaluated crystal quality and *c*-axis orientation (Figure 1c). The full-width at half-maximum (FWHM) values were 3.85° for $Al_{0.75}Sc_{0.25}N$ and 3.79° for $Al_{0.7}Sc_{0.3}N$, confirming well-oriented wurtzite crystalline phases. Considering that the FWHM of films produced by the sputtering oven is typically less than 2°, the observed FWHM of 3°–4° is relatively high. This can be attributed to the effect of increased thickness on crystallization quality: as thickness increases, columnar grains grow along the (0002) direction (Figure S1, Supporting Information), leading to accumulated grain boundaries and slight orientation deviations, thus broadening the FWHM. Furthermore, partial relaxation of interfacial stress in thicker films causes a wider distribution of lattice distortions, further increasing the FWHM. Atomic force microscopy (AFM) images (Figure 1d) showed root-mean-square roughness values of 1.60 nm for $Al_{0.75}Sc_{0.25}N$ and 1.83 nm for $Al_{0.7}Sc_{0.3}N$ over a 15×15 μm² area, indicating uniform and flat surface morphology.

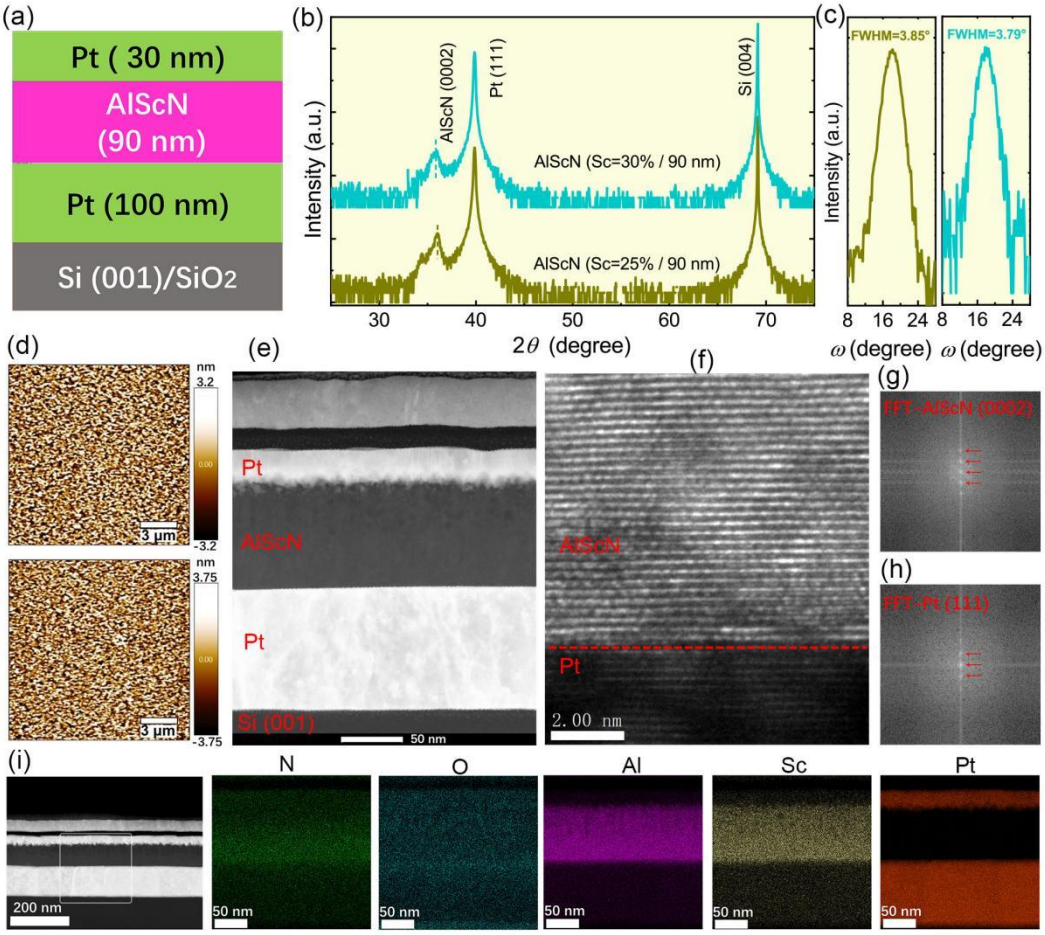

Figure 1. Structure characterization of AlScN (Sc=25% and 30%) films. (a) A schematic of sample stack for Pt/AlScN/Pt samples on SiO_2/Si(001). (b) XRD θ-2θ curves and (c) rocking curves of two Pt/AlScN (Sc=25% & 30)/Pt samples. (d) AFM images of two Pt/$Al_{0.75}Sc_{0.25}N$/Pt (up) and Pt/$Al_{0.7}Sc_{0.3}N$/Pt (down) samples. (e) Cross-sectional STEM image of representative Pt/AlScN(Sc=25%)/Pt sample. (f) STEM image showing the smooth AlScN/Pt (bottom electrode) interface and wurtzite (0002) planes of AlScN. The corresponding FFT images of (g) AlScN (0002) and (h) Pt(111). (i) STEM image and corresponding EDS element mapping of the Pt/AlScN(Sc=25%)/Pt heterostructure.

To assess the interface quality, element composition and microstructure of Pt/AlScN/Pt samples, STEM experiments were performed. Figure 1e displays the cross-sectional STEM image of the representative Pt/$Al_{0.75}Sc_{0.25}N$/Pt sample, clearly showing the three-layer structure

of Pt (~30 nm)-AlScN (~90 nm)-Pt (~100 nm) on the SiO_2/Si(100) substrate. The AlScN/Pt (bottom electrode, BE) interface is quite sharp, and the AlScN layer shows a homogeneous polycrystalline structure with obvious columnar grains appearing near the Pt top electrode (TE) interface (Figure S1, Supporting Information). A magnified STEM image (Figure 1f) highlights the smooth AlScN/Pt (BE) interface and the detailed wurtzite structure. The (0002) lattice fringes of the wurtzite structure with highly ordered atomic stacking sequence are visible and are oriented parallel to the substrate surface, which is similar to previously reported sputter-grown wurtzite AlScN film.[37] Fast Fourier Transformation (FFT) images in Figure 1g,h further validate the predominant orientation growth of Pt (111) and AlScN (0002). Energy dispersive X-ray spectroscopy (EDS) analysis in the region marked by the white box in Figure 1i reveals uniform distributions of nitrogen, oxygen, aluminum, scandium within the AlScN bulk layer, while platinum is concentrated in top and bottom parts. It should be noted that oxygen is unavoidable even in the vacuum experimental environment of TEM, the oxygen element in the EDS map here does not mean that the material is oxidized. Evidence of oxidation would manifest as uneven oxygen distribution at the AlScN surface. To determine the actual composition of $Al_{0.75}Sc_{0.25}N$, totally three different areas were analyzed. The results yielded an average Al/Sc ratio of 3.21, slightly deviating from the nominal composition (Figure S2, Supporting Information). Thus we still describe it with the nominal component $Al_{0.75}Sc_{0.25}N$.

2.2. FE switching demonstration for $Al_{1-x}Sc_xN$ capacitors

Subsequently, electrical characterizations were conducted to evaluate the ferroelectricity of fabricated Pt/AlScN/Pt capacitors at room temperature. **Figure 2**a presents the wurtzite-structured FE AlScN showing two stable polarization states of *M*-polar (Al,Sc-polar) (upper panel) and *N*-polar (lower panel).[3,8] To investigating FE switching, remanent polarization/displacement current density variations with applied voltage (P_r−V/J−V), positive

up and negative down (PUND) and retention measurements were performed on Pt/AlScN/Pt capacitors. A triangular waveform PUND bias sequence[40] at 10 kHz (Figure S3a, Supporting Information) was utilized to exclude non-switching contributions and extract P_r–V and J–V loops. The dimension of the square top electrodes was 15×15 μm^2, and all electrical measurements were done by applying voltages from the TE at room temperature. As shown in Figure 2b,c, two $Al_{1-x}Sc_xN$ (x=0.25 and 0.3) films show clear hysteresis loops and characteristic displacement current peaks, indicating distinct FE polarization switching. In particular, the well-closed and square-shaped P_r–E loops indicate uniform incorporation of Sc,[8,41] which is also directly related to the wurtzite structure that allows only 180° domain rotations.[8] It should be pointed out that there is a certain amount of noise in the J-V loops, which comes from the limitations of the measurement system, the heterogeneity of polycrystalline and environmental factors, rather than a problem of data validity. The P_r values are ~133 $\mu C/cm^2$ for $Al_{0.75}Sc_{0.25}N$ and ~128 $\mu C/cm^2$ for $Al_{0.7}Sc_{0.3}N$. The features of large P_r and hysteresis loop with a steep switching slop make $Al_{1-x}Sc_xN$ a promising material to enable ultra-high density FE random-access memory application. The average E_c value ($\overline{E_c} = (|E_c^+| + |E_c^-|)/2$) of $Al_{0.75}Sc_{0.25}N$ is ~39.35 V(~4.37 MV/cm), and that of $Al_{0.7}Sc_{0.3}N$ is ~33.15 V (~3.68 MV/cm). The lower average E_c value in $Al_{0.7}Sc_{0.3}N$ reflects the gradual decrease in switching barrier with increasing Sc content.[8,24,39]

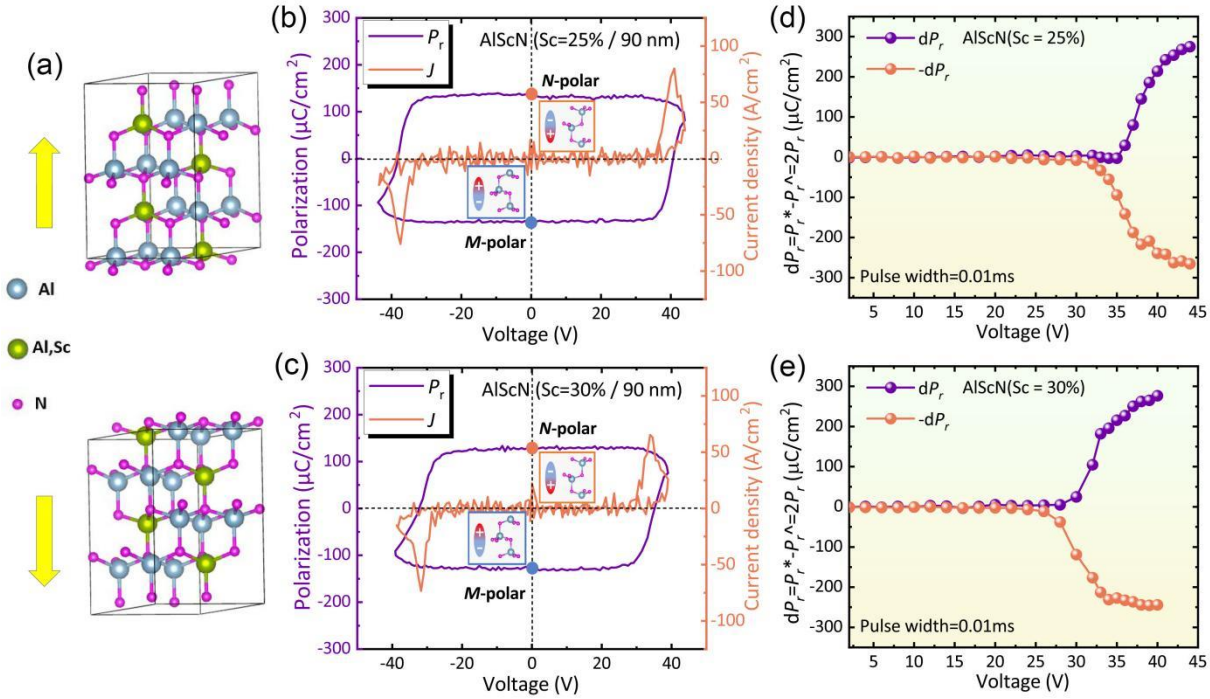

Figure 2. FE switching demonstration of AlScN (Sc=25% and 30%) films. (a) Wurtzite-structured FE AlScN showing two stable polarization states of *M*-Polar (upper panel) and *N*-polar (lower panel). Remanent P_r-*V* and *J*-*V* loops measured at 10 kHz for (b) 90-nm AlScN (Sc=25%) and (c) 90-nm AlScN (Sc=30%) samples. Electric field-dependent P_r recorded from standard pulsed-PUND measurement for (d) 90-nm AlScN (Sc=25%) and (e) 90-nm AlScN (Sc=30%) samples, showing saturation behavior in both branches.

To quantify the P_r more precisely, square pulsed PUND measurements[40,42] were further performed (Figure S3b, Supporting Information). During these measurements, the time-integrated switching currents in (P–U) and (N–D) correspond to positive and negative $2P_r$ values for a specific electric field, respectively. As an example, Figure S3b shows the current transients during PUND measurement using square pulses at ±4.89 MV/cm (±44 V) for the $Pt/Al_{0.75}Sc_{0.25}N/Pt$ capacitor. Clear switching currents can be identified in the switching pulses P and N, while the current during the pulses U and D represents the non-switching current arising from leakage and dielectric responses.[40,43] Further, the voltage-dependent pulse PUND results are shown in Figure 2d,e for two AlScN capacitors. Both films exhibit good saturation

P_r values under the negative branch, but the saturation effect is not so good under the positive voltage, and there is a certain contribution of leakage current. This result is acceptable because in the $Al_{1-x}Sc_xN$ thin film, it is usually impossible to fully compensate for the leakage current through PUND measurement.[24] Moreover, it is impossible to saturate the polarization by continuously increasing the voltage. Since the electrical breakdown strength of the AlScN sample is very close to its E_c, the sample will be broken down. The P_r ~133 μC/cm^2 of $Al_{0.75}Sc_{0.25}N$ is larger than that of $Al_{0.7}Sc_{0.3}N$ (~128 μC/cm^2), which is consistent with the previously reported trend that P_r decreases with increasing Sc content.[8,39] Additionally, a retention test was performed on the representative Pt/$Al_{0.75}Sc_{0.25}N$/Pt capacitor to reveal the stability of wurtzite FE-AlScN (Figure S3c, Supporting Information). The P_r for both positive and negative directions shows negligible fluctuation over 10^5 s after electrical poling, indicating little polarization loss and strong stability of FE polarization. These results clearly suggest robust ferroelectricity of $Al_{1-x}Sc_xN$ capacitors.

2.3. Polarization switching kinetics under various driving voltages

Fundamentally, the utility of FE materials is derived from the ability of polarization switching by an external electric field by means of domain nucleation and growth.[44,45] Therefore, understanding the polarization switching kinetics of FE materials is critical to exploiting their reliable nanoelectronic device applications.[27] After proving the good FE properties of wurtzite nitride $Al_{1-x}Sc_xN$ films, we proceeded to explore the polarization switching kinetics via pulse switching measurements using a designed and modified PUND method[46] in Keithley 4200A-SCS parameter analyzer (See Experimental section and Figure S4, Supporting Information). The normalized polarization change ΔP in three Pt/$Al_{1-x}Sc_xN$/Pt capacitors as a function of applied switching pulse width (t_w) and amplitudes (V_p) at room temperature are depicted in **Figure 3**a–c.

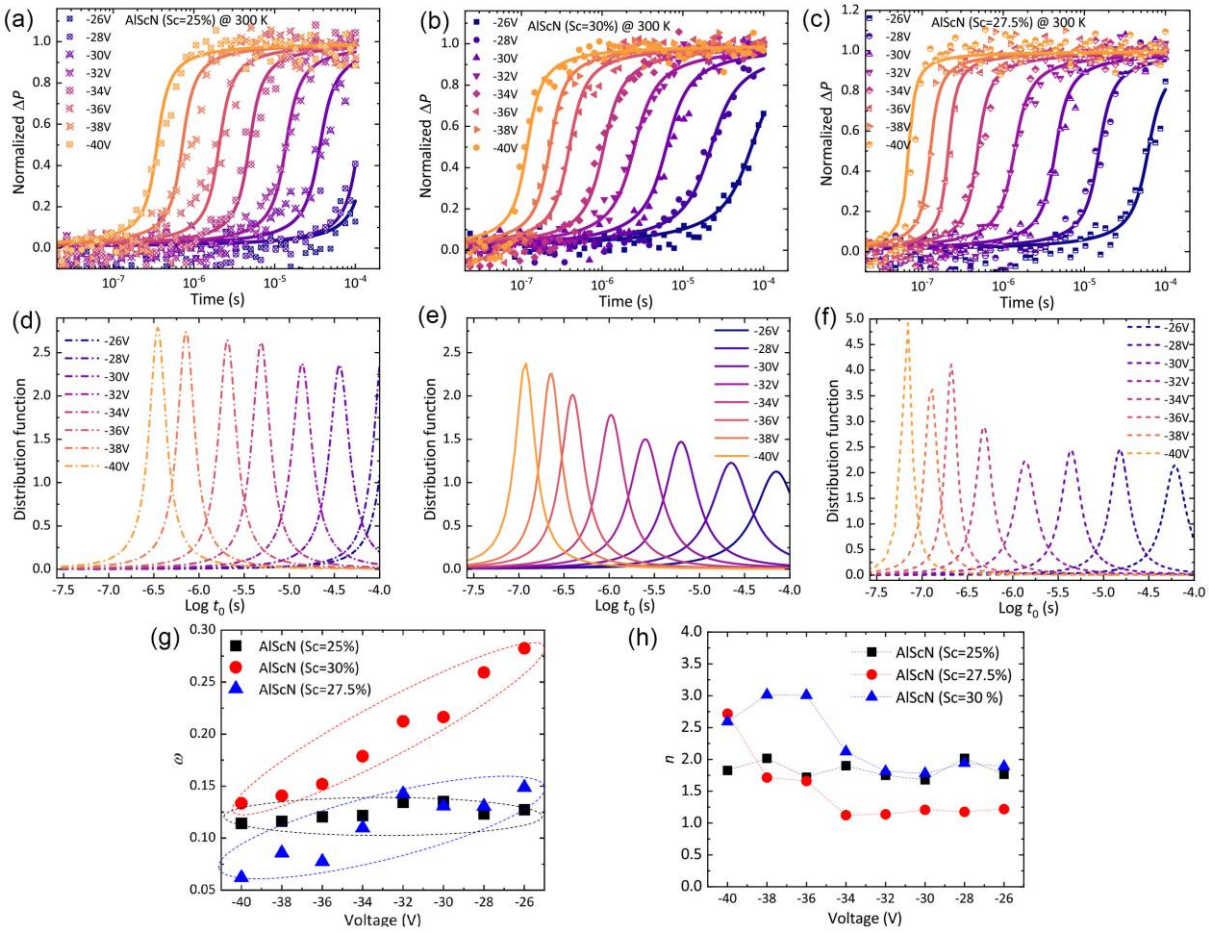

Figure 3. Polarization switching kinetics characterizations of $Al_{1-x}Sc_xN$ (x=0.25, 0.275 and 0.3) capacitors. Switchable normalized polarization ΔP as a function of pulse duration time under different pulse amplitudes (V_p) for the (a) $Al_{0.75}Sc_{0.25}N$, (b) $Al_{0.7}Sc_{0.3}N$ and (c) $Al_{0.725}Sc_{0.275}N$ samples. The solid lines are fittings according to the NLS model as discussed in the text. Lorentz distribution function for different voltages used in the fitting by the NLS model for the (d) $Al_{0.75}Sc_{0.25}N$, (e) $Al_{0.7}Sc_{0.3}N$ and (f) $Al_{0.725}Sc_{0.275}N$ samples, respectively. (g) The changing tendency of w as a function of applied voltages for the $Al_{0.75}Sc_{0.25}N$, $Al_{0.7}Sc_{0.3}N$ and $Al_{0.725}Sc_{0.275}N$ capacitors. (h) Summarized voltage dependent effective domain growth dimension n for $Al_{0.75}Sc_{0.25}N$, $Al_{0.7}Sc_{0.3}N$ and $Al_{0.725}Sc_{0.275}N$ samples based on KAI model.

In FE materials, polarization switching occurs through the nucleation of a reversed domain, followed by its subsequent growth. Two groundbreaking models, KAI model and NLS model, have been developed to explain the diverse polarization switching dynamics of FEs.[27,47–53] The

KAI model, based on the statistical theory of nucleation and unrestricted domain growth,[27,47–49] has been successfully applied to describe FE switching in uniformly polarized single crystals and epitaxial films.[47–50] However, it falls short in characterizing switching dynamics in less ideal systems like polycrystalline films.[51] To address this limitation, the NLS model offers an alternative approach. It assumes that FE capacitors comprise several regions, each exhibiting independent switching dynamics governed by nucleation time distributions. This model suggests that polarization reversal is primarily influenced by domain nucleation, with minimal domain propagation.[51–54] Both models can be represented in a general form as equation (1):

$$\Delta P(t) = 2P_s \int_{-\infty}^{+\infty} \left[1 - \exp\{-(t/t_0)^n\}\right] F(\log t_0)\, d\log t_0 \qquad (1)$$

Here, P_s is the spontaneous polarization, t_0 denotes the characteristic switching time for polarization switching evolution, $F(\log t_0)$ is the distribution function for $\log t_0$, and n represents the effective dimension of domain growth (e.g., $n = 2$ for thin films). The distinction between the two models lies in the specific form of the distribution function $F(\log t_0)$. In the NLS model, polarization switching is significantly influenced by defects that disrupt uniform domain nucleation, resulting in a Lorentzian distribution function of equation (2):

$$F(\log t_0) = \frac{A}{\pi}\left[\frac{w}{(\log t_0 - \log t_1)^2 + w^2}\right] \qquad (2)$$

Where A is a normalization constant, $2w$ is the full-width at half-maximum (FWHM), and $\log t_1$ is the center of the distribution. While for the KAI model, w is close to zero and the distribution function $F(\log t_0)$ reduces to a Dirac delta function. Thus the equation (1) of this model can be written as equation (3):

$$\Delta P(t) = 2P_s \left[1 - \exp\{-(t/t_0)^n\}\right] \qquad (3)$$

Therefore, the KAI model can be regarded as a special case of the NLS model. However, this mathematical equivalence under the limit of $w \rightarrow 0$ does not imply identical physical mechanisms. The KAI model inherently assumes unrestricted domain growth, while the NLS

model emphasizes nucleation-limited dynamics with suppressed domain propagation, as defined by their distinct physical premises.[51,52] For the sputtered polycrystalline AlScN samples, the NLS model is predominantly applied to analyze and fit the FE switching data of the two capacitors to ensure result comparability, as indicated by the solid lines in Figure 3a–c. The corresponding Lorentz distribution functions of the characteristic switching time for $Al_{0.75}Sc_{0.25}N$, $Al_{0.7}Sc_{0.3}N$ and $Al_{0.725}Sc_{0.275}N$ are depicted in Figure 3d–f, respectively. Note that we have also supplemented the plots of the numerical derivatives of the measured data on log*t* and the extracted NLS Lorentzian distribution functions for the $Al_{0.75}Sc_{0.25}N$ and $Al_{0.7}Sc_{0.3}N$ samples at different voltages, as shown in Figures S9 and S10, respectively. The numerical derivatives are highly consistent with the extracted NLS Lorentzian distribution functions, proving the high reliability of the extracted NLS Lorentzian distribution functions. At first glance, the NLS model fits the polarization switching kinetics data of three capacitors well. However, closer inspection of the Lorentz distribution functions reveals the switching mechanism variations caused by different Sc doping levels. For the $Al_{0.75}Sc_{0.25}N$ film, as V_P changes from –26 V to –40 V, the intensity of $F(\log t_0)$ shows minimal or no variation, stabilizing around ~2.5. Furthermore, the extracted w value remains consistently low, approximately 0.12, and exhibits negligible dependence on the applied V_P, as displayed in Figure 3g. These characteristics deviate from previous reports on FE materials fitted with the NLS model,[52,55] where both the intensity and w value typically vary obviously with applied voltage or electric field. Specifically, in the NLS model, w reflects the strength of the material's microscopic inhomogeneity. The almost constant $F(\log t_0)$ and small w (~0.12) values under different applied V_P (Figure 3d,g) reflects the high homogeneity of its nucleation activation energy distribution between the nucleating regions. This contradicts the core assumption of the NLS model (inhomogeneous nucleation dominance), but conforms to the uniform nucleation-free expansion mechanism of the KAI model. Furthermore, the Sc doping concentration x = 0.25 is close to the theoretical predicted mechanism transition threshold ($x \approx 0.22$–0.28)[21],

further supporting the dominance of the collective inversion mechanism (KAI) at low Sc concentrations. Therefore, the NLS mechanism does not adequately describe the switching kinetics of $Al_{0.75}Sc_{0.25}N$. Instead, the nearly constant *w* value aligns with the minimal variation in *n* from the KAI model, indicating that the switching dynamics of the $Al_{0.75}Sc_{0.25}N$ film predominantly follow the KAI mechanism. To confirm, we applied equation (3) from the KAI model to fit the switching kinetics data for the $Al_{0.75}Sc_{0.25}N$ capacitor (Figure S5, Supporting Information). The extracted domain growth dimension, *n*, remained approximately 2 across all voltages, as shown in Figure 3h. This finding corresponds to the two-dimensional in-plane propagation of switching domains, consistent with conventionally KAI-dominated FE films.[27,56]

For $Al_{0.7}Sc_{0.3}N$ samples, the switching characteristic differs due to the higher Sc doping concentration. As shown in Figure 3g, increasing the absolute value of V_p from 26 V to 40 V causes the intensity of the distribution function $F(\log t_0)$ to rise progressively from 1.1 to 2.4. Concurrently, the *w* value decreases gradually from ~0.28 to ~0.13, as shown in Figure 3g. Note that Lu et al. recently investigated polarization switching dynamics in 20 nm $Al_{0.72}Sc_{0.28}N$ films,[33] where the NLS mechanism dominated within the low voltage range (9 V to 11 V). In their study, the FWHM (2*w*) value similarly exhibited a gradual reduction from ~0.28 to ~0.12. In addition, we also added the KAI fittings and Avrami exponent *n* for the $Al_{0.7}Sc_{0.3}N$ film (Figure S6, Supporting Information). However, the fitting results of the KAI model were accompanied by unreasonable and small values of *n* ($n < 1.2$ when V_p is -26 V to -34 V) as well as partial fitting deviation (V_p is -36 V to -40 V), which indicates that the KAI model is not suitable for sputtered polycrystalline $Al_{0.7}Sc_{0.3}N$ film. In short, these observations collectively indicate that the $Al_{0.7}Sc_{0.3}N$ films demonstrate characteristic NLS-type switching behavior. In contrast to the KAI model, the NLS model assumes that the polarization switching is limited by the domain nucleation.[34,51–54] Moreover, the NLS model has been demonstrated to be applicable to polycrystalline films.[34,51–54] Therefore, it is plausible that the NLS-based

mechanism operates in sputtered polycrystalline AlScN films. Indeed, since the KAI and SNNG models were early reported, several experimental studies in 2024 have recently documented the presence or dominance of the NLS mechanism in AlScN capacitors.[32–34] However, given the relatively recent discovery of ferroelectricity in this class of materials, the correlation between polarization switching kinetics and varying Sc doping levels is still not fully explored, which is crucial for developing reliable devices with reduced E_c. Here, we experimentally identified a mutable polarization switching mechanism induced by Sc doping in FE wurtzite $Al_{1-x}Sc_xN$, providing a foundation for further material engineering.

In order to further clarify the switching mechanism crossover across the composition, we have added an additional composition point of AlScN (Sc=27.5%) film. The confirmation of ferroelectricity is presented in Figure S7 of Supporting Information and the polarization switching kinetics results are shown in Figures S7, Figure S8 and Figure 3. Figure 3c shows the polarization switching data and the fitting results based on the NLS model. The Lorentz distribution functions extracted at different voltages are presented in Figure 3f. Overall, the NLS model can fit the experimental data relatively well. As the absolute value of V_p increases from 26 V to 40 V, the intensity of the distribution function $F(\log t_0)$ rises from 2.2 to 4.9, while the w value decreases from ~0.15 to ~0.06 (Figure 3g). In the NLS model, w reflects the degree of the microscopic inhomogeneity. The w value changes with the applied voltage, which to some extent represents the inhomogeneity in the $Al_{0.725}Sc_{0.275}N$ thin film and is in line with the expectations of the NLS model. However, a more detailed analysis will reveal that: 1) At lower absolute V_p values (26–32 V), both $F(\log t_0)$ (~2.2) and w (~0.15) remain relatively stable; 2) At higher absolute V_p values (32–40 V), w decreases modestly but remains low, suggesting that the KAI model may also describe the switching behavior adequately.

Indeed, Figure S8c displays the polarization switching data and the fitting results based on the KAI model. The effective domain growth dimensions n derived at various voltages are presented in Figure S8d. We can find that the KAI model also provides a good fit. At lower

absolute value of V_p (26–34 V), n is approximately 2. At higher absolute voltages (34–40 V), n increases slightly to 2.5–3, still within the KAI-expected range ($n < 4$).[29] These results suggest that $Al_{0.725}Sc_{0.275}N$ aligns more closely with the KAI model.

Figure 3g,h compares w values from the NLS model and n values from the KAI model across different film compositions. Results suggest that $Al_{0.725}Sc_{0.275}N$ aligns more closely with the KAI model. However, compared with the $Al_{0.75}Sc_{0.25}N$ film, the inhomogeneity of the system has increased to a certain extent (the w value is changing overall, but the change amplitude is smaller than that of the $Al_{0.7}Sc_{0.3}N$ film). Therefore, the switching dynamics of the intermediate composition $Al_{0.725}Sc_{0.275}N$ film, which exhibits transitional switching behavior (suitable for both KAI and NLS), further illustrates that as the Sc content increases, the system inhomogeneity increases, which may lead to a change in the switching mechanism. This also directly supports the NLS switching behavior exhibited by $Al_{0.7}Sc_{0.3}N$.

2.4. Calculation and analysis of activation field versus Sc doping content in wurtzite $Al_{1-x}Sc_xN$.

Subsequently, we try to quantitatively analyze the center of switching time (log t_1) for $Al_{1-x}Sc_xN$ capacitors from the NLS fitting to calculate the FE switching activation field (E_a), a critical parameter for assessing energy consumption in FE switching. It is observed that t_1 decreases with an increase in the absolute value of applied V_p magnitude (Figure 3d-f). To quantify the relationship between them, we plotted Ln t_1 against of |1/E| in the **Figure 4**a. The data revealed a linear correlation, consistent with Merz's empirical law,[57] which is widely employed to describe FE polarization switching time, as expressed by the follow equation:

$$t_1 = t_\infty \exp\left(\frac{E_a}{E}\right) \quad (4)$$

where t_∞ is the lower limit of switching time and E_a is the activation field. From the linear fittings of Ln t_1 v.s. |1/E|, the activation field values for $Al_{0.75}Sc_{0.25}N$, $Al_{0.725}Sc_{0.275}N$ and $Al_{0.7}Sc_{0.3}N$ capacitors were determined to be ~63.15 MV/cm, ~55.5 MV/cm and ~53.69 MV/cm,

respectively. Note that for the $Al_{0.75}Sc_{0.25}N$ sample, the KAI model fitting was also employed to calculate the activation field E_a , which is ~60.91 MV/cm (Figure S5b, Supporting Information). Nonetheless, the E_a value for $Al_{0.75}Sc_{0.25}N$ thin films does not change significantly, regardless of whether the NLS or KAI model is employed, which is consistent with prior report.[32] In comparison, the smaller E_a values for $Al_{0.725}Sc_{0.275}N$ and $Al_{0.7}Sc_{0.3}N$ samples, which has a higher Sc doping concentration, indicates the external field required for nucleation and domain propagation of reversed polarization is reduced. This reduction facilitates the easier alignment of dipoles. Importantly, this result experimentally confirms that increasing the Sc content in $Al_{1-x}Sc_xN$ induces a transition in the polarization switching mechanism—from a higher-energy barrier process dominated by domain growth to a lower-energy mechanism governed by nucleation, consistent with the NLS model.

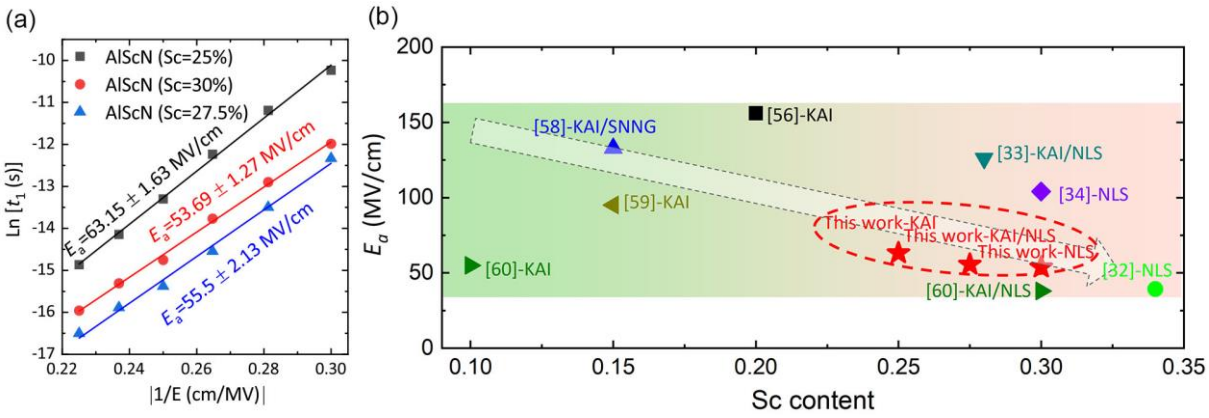

Figure 4. Calculation and analysis of activation field versus Sc doping content in wurtzite $Al_{1-x}Sc_xN$. (a) Calculation of activation field E_a from the electric-field dependence of the switching times obtained from NLS fitting for AlScN (Sc=25%), AlScN (Sc=27.5%) and AlScN (Sc=30%) capacitors. The solid black, red and blue curves are fitted by Merz's law of FE switching. (b) Summary and comparison of the activation field E_a values versus Sc contents obtained from various FE switching models for the $Al_{1-x}Sc_xN$ system.

Currently, the polarization switching kinetics mechanisms reported by various research groups are inconsistent or controversial. One possible reason for this discrepancy could be the

variation in Sc doping levels. To address, we summarize and compare our findings with the activation field E_a values derived from different FE switching kinetics models for the $Al_{1-x}Sc_xN$ system as reported in recent literature.[32–34,56,58–60] The data are summarized in Table S1 of Supporting Information and illustrated in Figure 4b. Three key points can be drawn from Figure 4b. First, the activation field of the $Al_{1-x}Sc_xN$ system (indicated by the shaded region) is significantly higher than that of the conventional PZT and $Hf_{1-x}Zr_xO_2$ systems by at least one order of magnitude.[32] Second, the E_a values extracted from our $Al_{1-x}Sc_xN$ (x = 0.25, 0.275 and 0.3) samples align closely with values reported in other studies, all falling within the shaded region. Most significantly, the combined results in Figure 4b reveal an overall decline in the FE activation field with increasing Sc doping concentration. Notably, a critical Sc content of approximately 0.25 appears to exist, beyond which the polarization switching mechanism transitions from the KAI to the NLS model. Note that this result, i.e., a critical Sc content of 0.25, is surprisingly consistent with the recent theoretical calculations of FE switching mechanism in $Al_{1-x}Sc_xN$ at the atomic scale by Lee et al., who also found that in $Al_{1-x}Sc_xN$, as x increases to around ($0.22 < x < 0.28$), the polarization switching path changes from a collective mechanism to a individual tetrahedral inversion mechanism with lower barrier.[21] Overall, this observation strongly supports our experimental conclusions.

2.5. Mechanistic understanding of the Sc-induced mutable polarization characteristics.

Nitride-based FE wurtzites are an emerging family of crystals that are highly attractive as switching materials for modern microelectronics. Understanding the FE switching mechanisms and dynamics in $Al_{1-x}Sc_xN$ offers valuable insights for optimizing wurtzite FEs and enhancing their reliability in practical applications. The changes in switching kinetics mechanism caused by increasing Sc doping concentrations can be explained through two key factors. Firstly, increasing Sc content raises the system's average bond ionicity. The FE response of $Al_{1-x}Sc_xN$ is influenced by the contrast between ionic Sc–N bonds and covalent Al–

N sp^3 bonds.[38] Greater Sc doping reduces the bond directionality by increasing bond ionicity,[38] which lowers the energy barrier for polarization reversal and facilitates the transition to the NLS mechanism. Secondly, Sc doping enhances the formation of nucleation sites. Acting as point defects, substitutional Sc dopants affect polarization switching kinetics through two ways:[31,34,35] (i) by serving as nucleation centers for FE switching;[34,35] (ii) by acting as pinning sites for moving domain walls and transformation fronts.[34,61] While domain wall pinning generally impedes FE switching, slows down the switching speed, and increases the switching energy barrier, the $Al_{0.725}Sc_{0.275}N$ and $Al_{0.7}Sc_{0.3}N$ sample exhibit the reduced energy barrier with higher Sc doping. This indicates that the pinning effect does not dominate the observed changes in switching mechanism. Notably, the increase in Sc dopants creates additional nucleation sites (Figure 5b), which accelerates nucleation and decreases the energy barrier, thereby promoting FE switching and driving the shift from KAI to NLS mechanisms.

Building on this analysis, we further present an energetic perspective to illustrate the mutable switching mechanisms occurring in the $Al_{1-x}Sc_xN$ wurtize FEs. The FE bistability arises from a double-well Gibbs free energy curve. The double-well potential is now defined using the Landau-Devonshire model for ferroelectrics: $U(P)= \alpha P^2 + \beta P^2+...$, where P is polarization, α and β are the coefficients of the second and fourth order terms dependent on Sc doping. This formalism aligns with first-principles calculations for wurtzite ferroelectric.[62,63] Figure **5a** depicts the FE double-well energy landscapes for two different switching mechanisms of KAI and NLS models. The barrier height and the energetic variation with respect to polarization states are determined by the path via which the switching occurs. Figure 5b depicts switching paths for various Sc doping levels. At lower Sc doping levels (e.g., $Al_{0.75}Sc_{0.25}N$), the switching follows the classical KAI path with nucleation and domain growth, characterized by a higher energy barrier, ΔE_1, as shown in Figure 5a. Figure 5c illustrates the KAI-based switching process,[27,29,58] involving the nucleation, the forward domain growth, the subsequent sideways growth and impingement. In contrast, with increasing Sc concentrations

(e.g., $Al_{0.7}Sc_{0.3}N$), the Sc dopants act as nucleation centers, as highlighted in Figure 5b, and the NLS path becomes dominant, resulting in a lower energy barrier ΔE_2 ($\Delta E_2 < \Delta E_1$). In Figure 5d, we also graphically illustrate the FE polarization reversal process based on the NLS model,[29,52,58] including the nucleation incubation stage, the increase of nucleation sites and the continues nucleation until the final reversal.

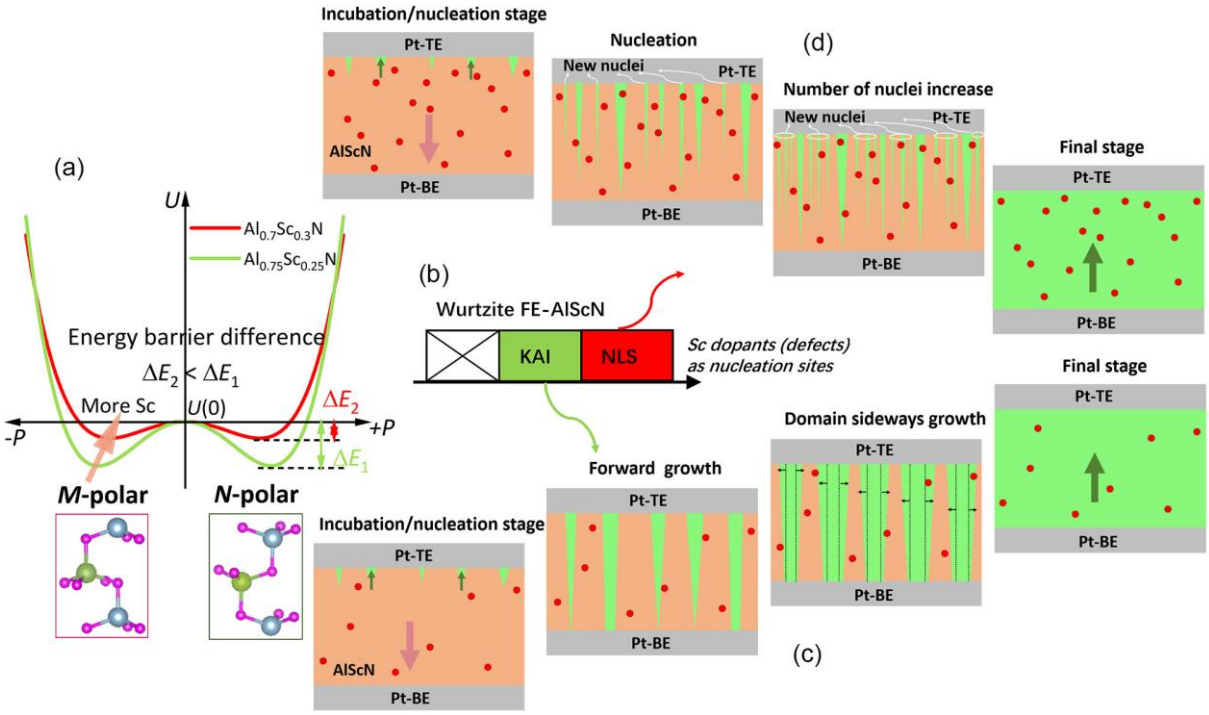

Figure 5. Schematic illustration of the Sc-doping-induced mutable polarization switching mechanism in wurtzite $Al_{1-x}Sc_xN$ from an energy perspective. (a) Schematic representation of flattening of the asymmetric FE double potential energy landscape with an external electric field favoring *M*-polar polarization due to more Sc doping concentration in wurtzite $Al_{1-x}Sc_xN$. (b) Illustration of the increase of Sc doping content in wurtzite-structured FE nitrides acts as nucleation sites and causes the mutable switching mechanism. (c) Schematic of polarization switching mechanism based on KAI model with nucleation followed by domain forward growth, sideways growth and impingement. (d) Schematic illustration of polarization switching mechanism based on NLS model with incubation stage, the increase of nucleation sites and

continues nucleation until final switching. The solid red circles represent Sc dopants, and different numbers of circles represent differences in the concentration of Sc doping in $Al_{1-x}Sc_xN$.

Notably, the rise in Sc content shifts the switching kinetics mechanism from KAI to NLS. This finding aligns, to some extent, with the significant theoretical effort of Lee et al., who calculated switching behaviors in $Al_{1-x}Sc_xN$ at the atomic scale.[21] Their study revealed that as Sc content increases to 0.22–0.28, the switching path transitions from a collective mechanism to a new low-barrier mechanism enabled by individual tetrahedral inversion. This individual inversion mechanism parallels nucleation-limited-switching mechanism, differing in that the NLS mechanism observed here pertains to macroscopic micrometer-scale capacitors. In any case, the results demonstrate that Sc content significantly influences switching mechanisms in $Al_{1-x}Sc_xN$, providing a foundation for future exploration.

3. Conclusion

In summary, we have fabricated Pt/$Al_{1-x}Sc_xN$ (x = 0.25, 0.275 and 0.3)/Pt sandwich FE heterostructures, and characterized their microstructure and robust ferroelectricity. In particular, this work demonstrates a mutable polarization switching kinetics mechanism in thin films of wurtzite FE $Al_{1-x}Sc_xN$ (x = 0.25, 0.275 and 0.3) achieved by Sc doping. Our data suggest that the classical nucleation and domain growth mechanism described by KAI model is valid for $Al_{0.75}Sc_{0.25}N$ with the relatively lower Sc concentration. Interestingly, the polarization switching mechanism is influenced by Sc doping levels, where increased Sc doping content (e.g., $Al_{0.7}Sc_{0.3}N$) accelerates nucleation, reduces the coercive field and FE switching energy barrier and favors a NLS process. The current work broadens the understanding of polarization switching kinetics and mechanisms in $Al_{1-x}Sc_xN$, and paves the way for potential applications of emerging wurtzite nitride-based FE materials.

4. Experimental Section

Thin Film Growth: The Pt/AlScN/Pt trilayers were deposited by AJA magnetron sputtering on SiO_2/Si(100) substrates. Before growing the sample, the base pressure in the chamber needs to be maintained better than 3×10^{-8} Torr at room temperature. Then, increase the substrate temperature to 500 ℃ and wait for 45 minutes to clean the substrate surface and perform temperature stabilization. To start with, a 100-nm-thick Pt film was first grown as a bottom electrode (BE) at 500 ℃ under 5 mTorr argon atmosphere by DC mode on the top of SiO_2/Si(100) substrate. Next, the substrate temperature was reduced to 350 ℃ to grow $Al_{1-x}Sc_xN$ (x=0.25 & 0.3) films. The 90-nm-thick $Al_{1-x}Sc_xN$ films with x=25% and 30% were deposited through RF magnetron sputtering using the $Al_{0.75}Sc_{0.25}$ and $Al_{0.7}Sc_{0.3}$ alloy targets with diameters of 2 inches under 3.5 mTorr pure nitrogen atmosphere. Then, in order to eliminate surface oxidation, a Pt film of about 30 nm was *in-situ* deposited on the upper surface of $Al_{1-x}Sc_xN$ at 350 ℃ as the top electrode (TE). Throughout the process, the substrate is continuously rotated for film deposition. Film thickness was controlled by the deposition time without an obvious change in composition.

Capacitor Device Fabrication: First, the Pt/AlScN/Pt sample was cleaned in acetone, methanol, and deionized water. Then, a lithographic step was performed to pattern the TE in squared structure with different areas (from 225 μm^2 to 2500 μm^2). The lithography was performed using an Ultraviolet Mask-less Lithography machine (TuoTuo Technology). Argon ion etching was performed after the laser lithographic development was completed. Through the already explored etching rate, it can ensure that the top ~30 nm Pt film is etched, and finally the separated top electrode is formed.

Microstructural Characterizations: The crystal structure of $Al_{1-x}Sc_xN$ (x=0.25 & 0.3) films was characterized by synchrotron X-ray diffraction (XRD) using a four-circle diffractometer with an X-ray wavelength of 1.5406 Å at the Singapore Synchrotron Light Source (SSLS). Surface

morphology measurements were carried out at room temperature utilizing a commercial scanning probe microscope (Asylum Research MFP-3D instrument). Transmission electron microscopy (TEM) characterization and image acquisition were performed using an FEI Titan 80–300 TEM system operating at a 200 kV accelerating voltage. Cross-section samples were prepared using the focused ion beam (FIB) system (FEI Helios Nanolab 450S).

Electrical Properties Measurements: The FE properties (Remanent *P-E* and *J-E* loops, PUND measurements and retention tests) were evaluated using a Radiant Precision Multiferroic II tester driven from TE operated at room temperature. The polarization switching kinetics were assessed through modified positive–up–negative–down (PUND) measurements[46] using a Keithley 4200A-SCS semiconductor parameter analyzer paired with a 4225-PMU pulse measurement unit. The modified PUND sequence employed for polarization change (ΔP) measurements is illustrated in Figure S4. In this approach, the initial positive voltage pulse (P) aligns the FE polarization in one direction. To isolate the purely FE component, a subsequent positive pulse (U) is applied, which eliminates non-switching contributions, such as dielectric charging and leakage. The net FE polarization is then calculated as $P_1 = \int (I_P - I_U)dt / A$, where I_P and I_U are the output currents corresponding to the P and U pulses, respectively, and A represents the capacitor device area. Following this, a third voltage pulse in the opposite direction (highlighted by the red rectangle in Figure S4) is applied. By adjusting the amplitude (V_P) and duration (t_w) of this pulse, the amount of switched polarization (ΔP) can be modulated. Finally, two negative voltage pulses (negative, N, and down, D) are used to calculate how much polarization was left to be switched ($P_2 = \int (I_N - I_D)dt / A$, where I_N and I_D are the output currents after the N and D pulses. This procedure allows the determination of the switched polarization ($\Delta P = P_1 - P_2$) after various switching pulses. Note that the intermediate rectangular pulse's effect on ΔP can alternatively be derived by integrating the measured

current over time, as with P_1 and P_2. However, the chosen method minimizes inaccuracies linked to short and small-amplitude pulses.

Supporting Information

Supporting Information is available from the Wiley Online Library or from the author.

Acknowledgements

This research is supported by A*STAR RIE2020, Advanced Manufacturing and Engineering (AME) Programmatic Grant-A20G9b0135, the Singapore Ministry of Education MOE-T2EP50121-0011, MOE Tier 1: 22-4888-A0001.

Received: ((will be filled in by the editorial staff))
Revised: ((will be filled in by the editorial staff))
Published online: ((will be filled in by the editorial staff))

Conflict of Interest

The authors declare no conflict of interest.

Data Availability Statement

The data that support the findings of this study are available from the corresponding author upon reasonable request.

References

[1] J. F. Scott, *Science* **2007**, *315*, 954–959.

[2] Z. Liu, H. Wang, M. Li, L. Tao, T. R. Paudel, H. Yu, Y. Wang, S. Hong, M. Zhang, Z. Ren, Y. Xie, E. Y. Tsymbal, J. Chen, Z. Zhang, H. Tian, *Nature* **2023**, *613*, 656–661.

[3] K.-H. Kim, I. Karpov, R. H. Olsson III, D. Jariwala, *Nat. Nanotechnol.* **2023**, *18*, 422–441.

[4] L. W. Martin, A, M. Rappe, *Nat. Rev. Mater.* **2017**, *2*, 16087.

[5] R. Guo, W. Lin, X. Yan, T. Venkatesan, J. Chen, *Appl. Phys. Rev.* **2020**, *7*, 011304.

[6] H. Lu, C.-W. Bark, D. Esque de los Ojos, J. Alcala, C. B. Eom, G. Catalan, A. Gruverman, *Science* **2012**, *336*, 59–61.

[7] X.-K. Wei, N. Domingo, Y. Sun, N. Balke, R. E. Dunin-Borkowski, J. Mayer, *Adv. Energy Mater.* **2022**, *12*, 2201199.

[8] S. Fichtner, N. Wolff, F. Lofink, L. Kienle, B. Wagner, *J. Appl. Phys.* **2019**, *125*, 114103.

[9] J. Hayden, M. D. Hossain, Y. Xiong, K. Ferri, W. Zhu, M. V. Imperatore, N. Giebink, S. Trolier-McKinstry, I. Dabo, J.-P. Maria, *Phys. Rev. Mater.* **2021**, *5*, 044412.

[10] D. Wang, P. Wang, B. Wang, Z. Mi, *Appl. Phys. Lett.* **2021**, *119*, 111902.

[11] K. Ferri, S. Bachu, W. Zhu, M. Imperatore, J. Hayden, N. Alem, N. Giebink, S. Trolier-McKinstry, J.-P. Maria, *J. Appl. Phys.* **2021**, *130*, 044101.

[12] D. Wang, S. Mondal, J. Liu, M. Hu, P. Wang, S. Yang, D. Wang, Y. Xiao, Y. Wu, T. Ma, Z. Mi, *Appl. Phys. Lett.* **2023**, *123*, 033504.

[13] T. Mikolajick, S. Slesazeck, H. Mulaosmanovic, M. H. Park, S. Fichtner, P. D. Lomenzo, M. Hoffmann, U. Schroeder, *J. Appl. Phys.* **2021**, *129*, 100901.

[14] U. Schroeder, M. H. Park, T. Mikolajick, C. S. Hwang, *Nat. Rev. Mater.* **2022**, *7*, 653–669.

[15] S. Shi, H. Xi, T. Cao, W. Lin, Z. Liu, J. Niu, D. Lan, C. Zhou, J. Cao, H. Su, T. Zhao, P. Yang, Y. Zhu, X. Yan, E. Y. Tsymbal, H. Tian. J. Chen, *Nat. Commun.* **2023**, *14*, 1780.

[16] S. Calderon V, J. Hayden, S. M. Baksa, W. Tzou, S. Trolier-McKinstry, I. Dabo, J.-P. Maria, E. C. Dickey, *Science* **2023**, *380*, 1034–1038.

[17] K.-H. Kim, S. Oh, M. M. A. Fiagbenu, J. Zheng, P. Musavigharavi, P. Kumar, N. Trainor, A. Aljarb, Y. Wan, H. M. Kim, K. Katti, S. Song, G. Kim, Z. Tang, J.-H. Fu, M. Hakami, V.

Tung, J. M. Redwing, E. A. Stach, R. H. Olsson III, and D. Jariwala, *Nat. Nanotechnol.* **2023**, *18*, 1044–1050.

[18] P. Wang, D. Wang, S. Mondal, M. Hu, J. Liu, Z. Mi, *Semicond. Sci. Technol.* **2023**, *38*, 043002.

[19] C. Liu, Q. Wang, W. Yang, T. Cao, L. Chen, M. Li, F. Liu, D. K. Loke, J. Kang, Y. Zhu, *2021 IEEE International Electron Devices Meeting (IEDM)*, **2021**, 8.1.1−8.1.4. DOI: 10.1109/IEDM19574.2021.9720535.

[20] S. K. Ryoo, K. D. Kim, W. Choi, P. Sriboriboon, S. Heo, H. Seo, Y. H. Jang, J. W. Jeon, M. K. Yeom, S. H. Lee, H. S. Park, Y. Kim, C. S. Hwang, *Adv. Mater.* **2024**, *37*, 2413295.

[21] C.-W. Lee, K. Yazawa, A. Zakutayev, G. L. Brennecka, P. Gorai, *Sci. Adv.* **2024**, *10*, eadl0848.

[22] S. Yasuoka, R. Mizutani, R. Ota, T. Shiraishi, T. Shimizu, M. Uehara, H. Yamada, M. Akiyama, H. Funakubo, *ACS Appl. Electron. Mater.* **2022**, *4*, 5165–5170.

[23] K. Yazawa, D. Drury, A. Zakutayev, G. L. Brennecka, *Appl. Phys. Lett.* **2021**, *118*, 162903.

[24] G. Schönweger, A. Petraru, M. R. Islam, N. Wolff, B. Haas, A. Hammud, C. Koch, L. Kienle, H. Kohlstedt, S. Fichtner, *Adv. Funct. Mater.* **2022**, *32*, 2109632.

[25] H. Moriwake, R. Yokoi, A. Taguchi, T. Ogawa, C. A. J. Fisher, A. Kuwabara, Y. Sato, T. Shimizu, Y. Hamasaki, H. Takashima, M. Itoh, *APL Mater.* **2020**, *8*, 121102.

[26] C.-W. Lee, N. U. Din, K. Yazawa, G. L. Brennecka, A. Zakutayev, P. Gorai, *Matter* **2024**, *7*, 1644–1659.

[27] W. J. Hu, D.-M. Juo, L. You, J. Wang, Y.-C. Chen, Y.-H. Chu. T. Wu, *Sci. Rep.* **2014**, *4*, 4772.

[28] S. Fichtner, F. Lofink, B. Wagner, G. Schönweger, T.-N. Kreutzer, A. Petraru, H. Kohlstedt, *2020 Joint Conference of the IEEE International Frequency Control Symposium and International Symposium on Applications of Ferroelectrics (IFCS-ISAF)*, **2020**, 1–4. DOI: 10.1109/IFCS-ISAF41089.2020.9234883.

[29] K. Yazawa, J. Hayden, J.-P. Maria, W. Zhu, S. Trolier-McKinstry, A. Zakutayev, G. L. Brennecka, *Mater. Horiz.* **2023**, *10*, 2936–2944.

[30] D. Behrendt, A. Samanta, A. M. Rappe, *Arxiv* **2024**, arXiv:2410.18816.

[31] A. Krishnamoorthy, S. C. Tiwari, A. Nakano, R. K. Kalia, P. Vashishta, *Nanotechnology*, **2021**, *32*, 49LT02.

[32] T. Y. Lee, M. S. Song, J. W. Cho, I. H. Choi, C. An, J. S. Lee, S. C. Chae, *Adv. Electron. Mater.* **2024**, *10*, 2300591.

[33] H. Lu, G. Schönweger, A. Petraru, H. Kohlstedt, S. Fichtner, A. Gruverman, *Adv. Funct. Mater.* **2024**, *34*, 2315269.

[34] J. Gao, Y.-C. Chien, L. Li, H. K. Lee, S. Samanta, B. Varghese, H. Xiang, M. Li, C. Liu, Y. Zhu, L. Chen, K.-W. Ang, *Small* **2024**, *20*, 2404711.

[35] S. Jesse, B. J. Rodriguez, S. Choudhury, A. P. Baddorf, I. Vrejoiu, D. Hesse, M. Alexe, E. A. Eliseev, A. N. Morozovska, J. Zhang, L.-Q. Chen, S. V. Kalinin, *Nat. Mater.* **2008**, *7*, 209–215.

[36] R. Guido, P. D. Lomenzo, M. R. Islam, N. Wolff, M. Gremmel, G. Schönweger, H. Kohlstedt, L. Kienle, T. Mikolajick, S. Fichtner, U. Schroeder, *ACS Appl. Mater. Interfaces* **2023**, *15*, 7030–7043.

[37] P. Musavigharavi, A. C. Meng, D. Wang, J. Zheng, A. C. Foucher, R. H. Olsson III, E. A. Stach, *J. Phys. Chem. C* **2021**, *125*, 14394.

[38] K. Yazawa, J. S. Mangum, P. Gorai, G. L. Brennecka, A. Zakutayev, *J. Mater. Chem. C* **2022**, *10*, 17557–17566.

[39] S. Yasuoka, T. Shimizu, A. Tateyama, M. Uehara, H. Yamada, M. Akiyama, Y. Hiranaga, Y. Cho, H. Funakubo, *J. Appl. Phys.* **2020**, *128*, 114103.

[40] P. Wang, D. Wang, S. Mondal, Z. Mi, *Appl. Phys. Lett.* **2022**, *121*, 023501.

[41] P. Wang, D. Wang, N. M. Vu, T. Chiang, J. T. Heron, Z. Mi, *Appl. Phys. Lett.* **2021**, *118*, 223504.

[42] P. Wang, D. Wang, S. Mondal, M. Hu, Y. Wu, T. Ma, Z. Mi, *ACS Appl. Mater. Interfaces* **2023**, *15*, 18022–18031.

[43] D. Wang, J. Zheng, P. Musavigharavi, W. Zhu, A. C. Foucher, S. E. TrolierMcKinstry, E. A. Stach, R. H. Olsson, *IEEE Electron Device Lett.* **2020**, *41*, 1774.

[44] C. T. Nelson, P. Gao, J. R. Jokisaari, C. Heikes, C. Adamo, A. Melville, S.-H. Baek, C. M. Folkman, B. Winchester, Y. Gu, Y. Liu, K. Zhang, E. Wang, J. Li, L.-Q. Chen, C.-B. Eom, D. G. Schlom, X. Pan, *Science* **2011**, *334*, 968–971.

[45] Y.-H. Shin, I. Grinberg, I-W. Chen, A. M. Rappe, *Nature* **2007**, *449*, 881–884.

[46] Y. Wei, G. Vats, B. Noheda, *Neuromorph. Comput. Eng.* **2022**, *2*, 044007.

[47] H. Orihara, S. Hashimoto, Y. Ishibashi, *J. Phys. Soc. Japan* **1994**, *63*, 1031–1035.

[48] Y. Ishibashi, Y. Takagi, *J. Phys. Soc. Japan* **1971**, *31*, 506–510.

[49] V. Shur, E. Rumyantsev, S. Makarov, *J. Appl. Phys.* **1998**, *84*, 445–451.

[50] Y. W. So, D. J. Kim, T. W. Noh, J. G. Yoon, T. K. Song, *Appl. Phys. Lett.* **2005**, *86*, 092905.

[51] A. K. Tagantsev, I. Stolichnov, N. Setter, J. S. Cross, M. Tsukada, *Phys. Rev. B* **2002**, *66*, 214109.

[52] J. Y. Jo, H. S. Han, J.-G. Yoon, T. K. Song, S.-H. Kim, T. W. Noh, *Phys. Rev. Lett.* **2007**, *99*, 267602.

[53] X. J. Lou, *J. Appl. Phys.* **2009**, *105*, 094112.

[54] I. Stolichnov, A. Tagantsev, N. Setter, J. S. Cross, M. Tsukada, *Appl. Phys. Lett.* **2003**, *83*, 3362–3364.

[55] Y.-C. Li, T. Huang, X.-X. Li, X.-N. Zhu, D. W. Zhang, H.-L. Lu, *Nano Lett.* **2024**, *24*, 6585–6591.

[56] S. Yasuoka, R. Mizutani, R. Ota, T. Shiraishi, T. Shimizu, K. Okamoto, M. Uehara, H. Yamada, M. Akiyama, H. Funakubo, *Appl. Phys. Lett.* **2023**, *123*, 202902.

[57] W. J. Merz, *Phys. Rev.* **1954**, *95*, 690–698.

[58] R. Guido, H. Lu, P. D. Lomenzo, T. Mikolajick, A. Gruverman, U. Schroeder, *Adv. Sci.* **2024**, *11*, 2308797.

[59] R. Guido, X. Wang, B. Xu, R. Alcala, T. Mikolajick, U. Schroeder, P. D. Lomenzo, *ACS Appl. Mater. Interfaces* **2024**, *16*, 42415−42425.

[60] S. Yasuoka, T. Shimizu, K. Okamoto, N. Sun, S. Doko, N. Matsui, T. Irisawa, K. Tsunekawa, A. Gruverman, H. Funakubo, *Adv. Mater. Interfaces* **2024**, 2400627.

[61] S. M. Yang, T. H. Kim, J.-G. Yoon, T. W. Noh, *Adv. Funct. Mater.* **2012**, *22*, 2310−2317.

[62] K. Yazawa, A. Zakutayev, G. L. Brennecka, Appl. Phys. Lett. 2022, 121, 042902.

[63] H. Wang, N. Adamski, S. Mu, C. G. Walle, J. Appl. Phys. 2021, 130, 104101.